Chapter 3. Ferroelectric/ferroelastic domain evolution under mechanical loading

Ferroelastic domain evolution under compressive loading was observed in a near-morphotropic polycrystalline PZT ceramic using PFM. A micromechanical test rig was set up in the scanning probe microscope to observe domain structures *in situ* during compression testing. The evolution processes observed from PFM images include overwriting of one lamellation by a differently oriented lamellation, domain wall motion in a herringbone-like domain structure, and the broadening of lamellae. Using EBSD and PFM data, it was confirmed that switching processes generally follow a primary principle: that positive work is done by external loads. However, this can occur by a combination of energetically favourable and unfavourable processes happening concurrently. The evidence suggests that switching processes are significantly constrained by pre-existing domain structures. A simple model of ferroelectric/ferroelastic switching was employed to discuss the evolution mechanisms. The research presented in this chapter was published as follows:

Kim KL, Huber JE. *In situ* observation of ferroelastic domain evolution in a near-morphotropic $Pb(Zr,Ti)O_3$ ceramic by piezoresponse force microscopy. J Eur Ceram Soc 2015;35:1459–68.

3.1 Introduction and literature review

Ferroelastic domain switching involves the rearrangement of domains by externally applied mechanical stress and is evident from macroscopic measurements [5–8]. For example, the compressive stress-strain curve and stress-electric displacement curve of typical ferroelectrics can be attributed to ferroelastic domain switching. From macroscopic observations, Hwang *et al*. [6] proposed a switching criterion which states that the work done by external loads must exceed a critical threshold value for switching to occur. Similar switching rules have been used as the basis of several electro-mechanical constitutive models [83,84,117]. However, to date there is relatively little direct evidence at the microscopic scale to indicate the mechanisms by which the switching process proceeds. This is of significance because the process may be affected by particular arrangements of ceramic grains and domains. Then macroscopic switching rules may not accurately reflect what happens at the microscopic scale.

One major source of microscopic evidence for switching processes has been the use of neutron/X-ray diffraction to indicate reorientation of the crystal lattice [64,65]. For example, 90° domain switching in PZT caused by compressive loading was characterized using X-ray diffraction and EBSD, supporting the hypothesis that compressive stress causes switching towards domains polarized orthogonal to the loading axis [58]. These studies give insight into the microscopic switching process but typically do not resolve the individual domains. Figure 3.1 shows a series of EBSD inverse pole figure taken from polycrystalline PZT during compressive loading in five loading steps [58]. However, the resolution and the precision of the technique are not sufficient to study the evolution of domain patterns in each grain.

The use of optical microscopy to observe large domains in ferroelectrics is also well known [30,35,41,54]. Potnis *et al.* [54] have used optical microscopy to observe the

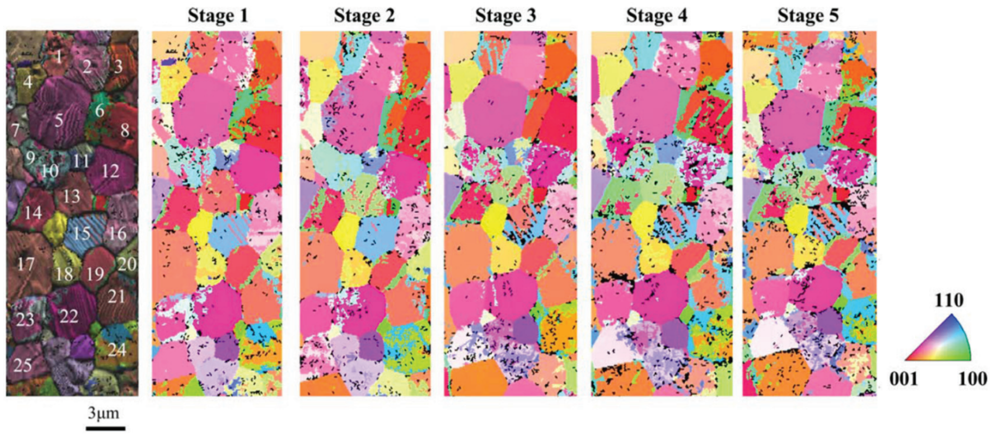

Figure 3.1: Domain evolution process by mechanical loading in polycrystalline PZT using EBSD inverse pole figure (modified from [58]).

evolution of domain patterns at the scale of hundreds of microns in single crystalline $BaTiO_3$, see figure 3.2(a). However, optical microscopy is unsuitable for the nanometre scale domains found in fine-grained and opaque ceramics. A promising approach for imaging fine-scale domains is PFM [42,48,99,118–120]. For example, a lamellation at the scale of a few microns growing by compressive loading in single crystal $BaTiO_3$ was captured by Muñoz-Saldaña *et al*. [33] using AFM and PFM as figure 3.2(b) shows.

In the present work, PFM is used to study domain evolution processes in polycrystalline PZT under compressive loading. The resulting observations show diverse evolution processes of ferroelastic domain structures by mechanical stress. The prediction of the energetic switching criterion of Hwang *et al.* [6] is compared with microscopic observations of domain processes, and the theory of compatible domain patterns is used to assist in the interpretation of results. The key finding is that while switching processes generally follow energetic criteria in an overall sense, local events occur that are energetically unfavourable. The domain pattern is constrained to evolve from pre-existing structure and this requires the co-operative action of energetically favourable and unfavourable processes.

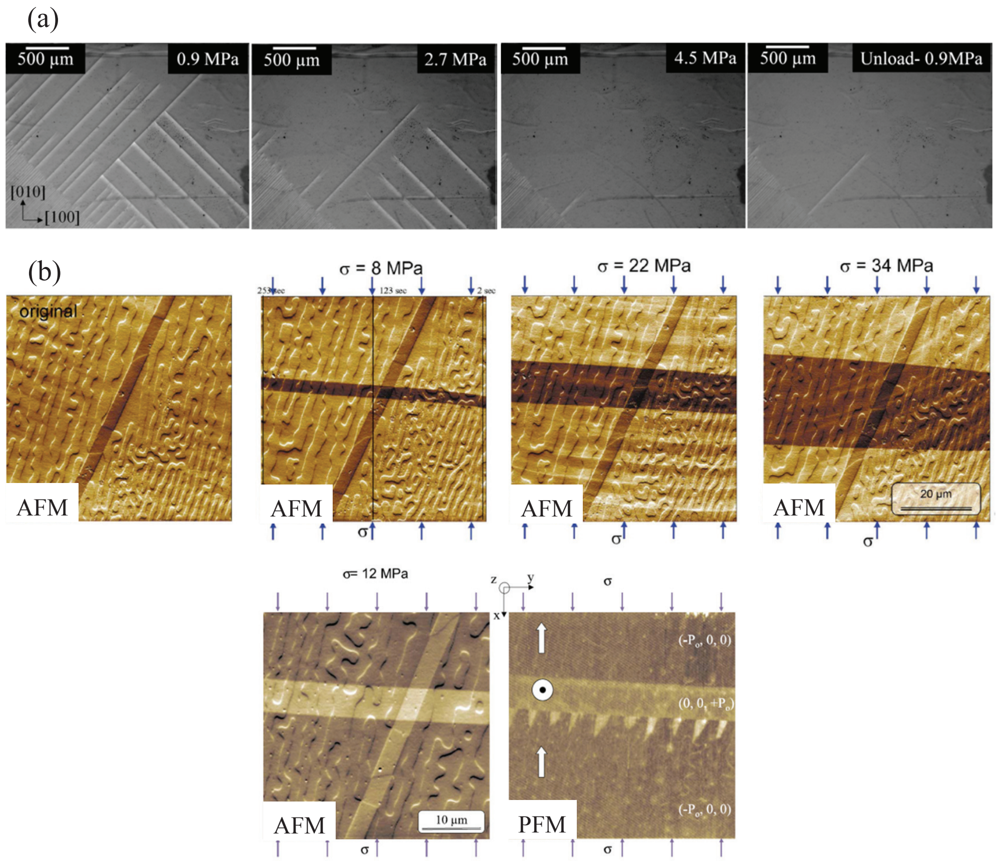

Figure 3.2: Domain evolution in single crystal barium titanate by compressive stress. (a) Evolution process of needle-like domains was observed by optical microscopy. (b) The four AFM images show nucleation and broadening processes of a domain. The two AFM and PFM images on the bottom row were taken when 12 MPa stress was applied. ((a) and (b) were modified from [54] and [33], respectively).

3.2 Material and method

Polycrystalline PZT near the morphotropic phase boundary, PZT-855, was used for compressive loading. In this composition, tetragonal and rhombohedral phases can coexist [15,16]. Bulk PZT was cut into a cuboid with $2\times4\times5$ mm^3 dimensions, and one of the 4×5 mm^2 faces was polished using 40 nm colloidal silica.

Ferroelectric domain structures were observed using VPFM in a Veeco Dimension 3100 nanoscope. VPFM images shown in this chapter have mixed phase and amplitude data, as discussed in chapter 1. Bruker SCM-PIC scanning probes were used with a 4–5 V amplitude of tip voltage, at 180–200 kHz near contact resonance frequency. Planar domain walls are observed as straight lines at the material surface, and the matching crystallographic planes were identified using EBSD. The EBSD measurements were carried out using an Evo LS 15 ESEM, operating in extended pressure mode at 10 Pa.

A micromechanical test rig (Deben Ltd., UK) with a 5 kN load cell was used for compressive loading. In-plane uniaxial compression was used to drive domain evolution processes which were then observed by PFM. Bulk materials are suitable for this type of study because the sample thickness is then sufficient to allow compression without causing severe bending. The PZT sample was clamped between the jaws in the rig, with a ceramic spacer between the sample and one of the jaws, providing open-circuit conditions. The test rig was linked to the sample stage of the scanning probe microscope allowing precision position control of the test rig, see figure 3.3.

A strain gauge was attached to the top surface of the sample, allowing the macroscopic strain parallel to the loading direction to be monitored during compression. Figure 3.4 shows the compressive loading process. Since the actual experiment took several hours to allow PFM scanning for many different regions, a simplified graph representing the measured strain and the corresponding actual stress levels are shown in this figure. A preliminary test was carried out by compressing the sample up to a 0.05% strain, to confirm no severe bending was occurring in the specimen and to test PFM scanning under compression. The test also confirmed that very little domain wall motion occurred at this strain level. Although spherical loading fixtures are often used for alignment in ceramic compression tests, these were found unsuitable because of the need for a high degree of stability during PFM scanning. Without spherical fixtures, some sample bending could occur during compression, and hence load cell measurements do

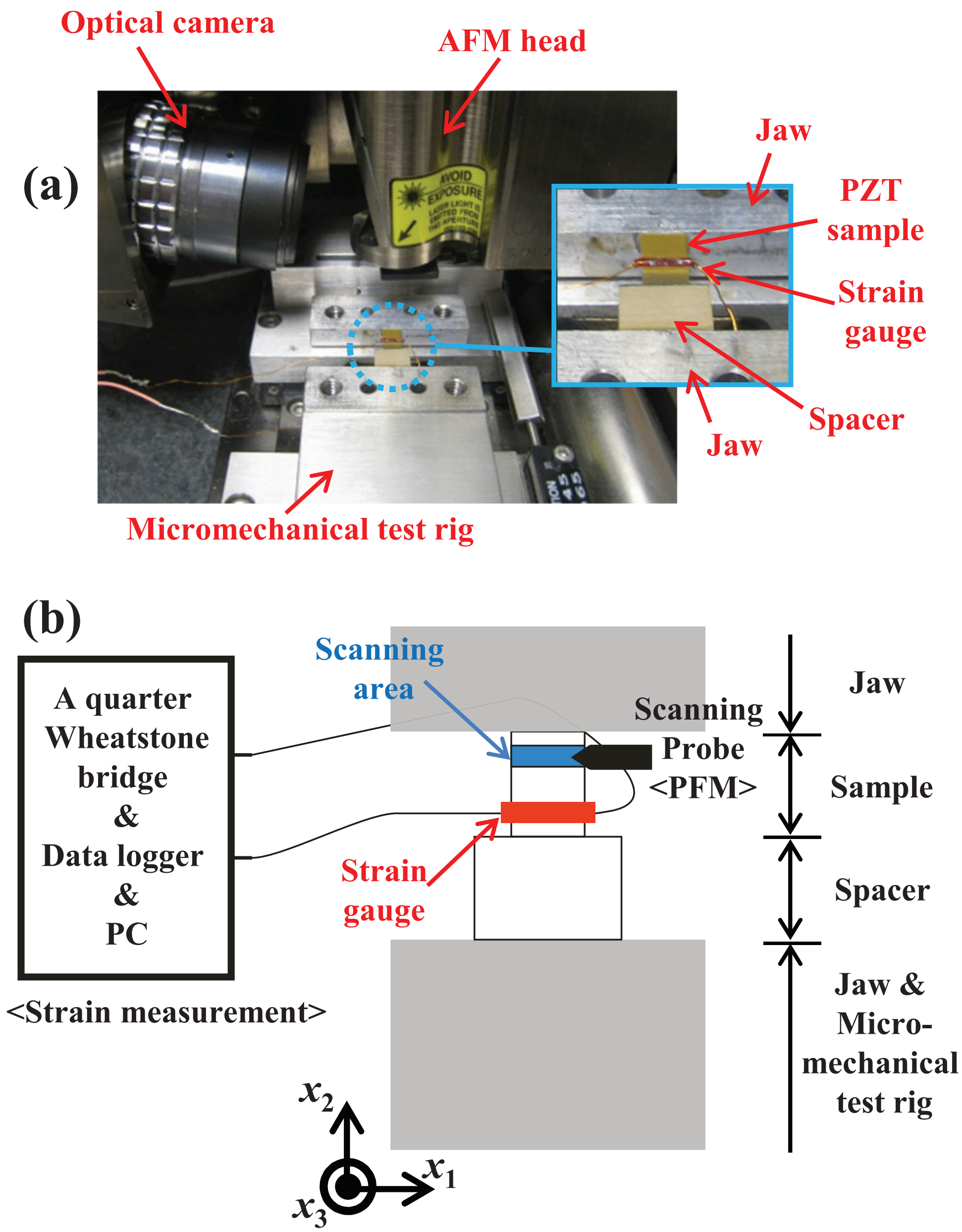

Figure 3.3: (a) The experimental arrangement, showing detail of the sample in the inset. (b) Schematic of the experimental set-up showing the location of the scanning probe.

not reliably indicate the stress at the sample surface. Thus, using another PZT sample, compression tests were conducted to examine variation in strain over the top surface. Two strain gauges were placed on the top surface, one being in the scanning area, and one in the position marked 'strain gauge' in figure 3.3(b). The result showed that very similar strains were generated from these two strain gauges, to within about 4×10^{-2}% strain,

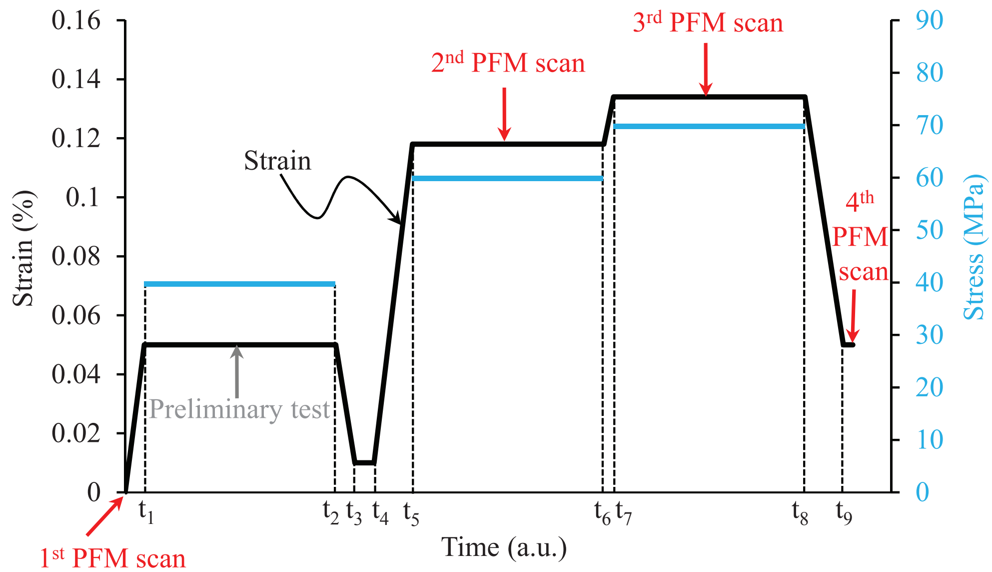

Figure 3.4: A mechanical loading process that shows the measured strain and the corresponding stress level.

indicating that strain generated within the top surface is very uniform in this experimental set-up. Then, the measured strain during *in situ* PFM observation was compared with a previous stress-strain curve measured on the same material using a pair of spherical loading fixtures, by Liu *et al*. [121] to give an approximate indication of the stress near the material surface.

Compressive loading was applied until the strain level reached about 0.118% strain (approximately 60 MPa stress), and PFM scans were taken while holding the material under load at this strain level. This loading target was based on prior observation that significant non-linear behaviour would occur by about 0.10% strain [7,8,121]. The loading was then increased to a strain level of 0.134% (approximately 70 MPa), and PFM images were again taken. Finally, the sample was unloaded, leaving a measured residual strain of about 0.05%, and PFM images of the final state were recorded.

To identify crystal orientations for the grains of interest, the sample was characterized using multiple instruments. Figures 3.5(a), (d) and (g) show EBSD inverse pole figures, figures 3.5(b), (e) and (h) AFM topography images, and figures 3.5(c), (f)

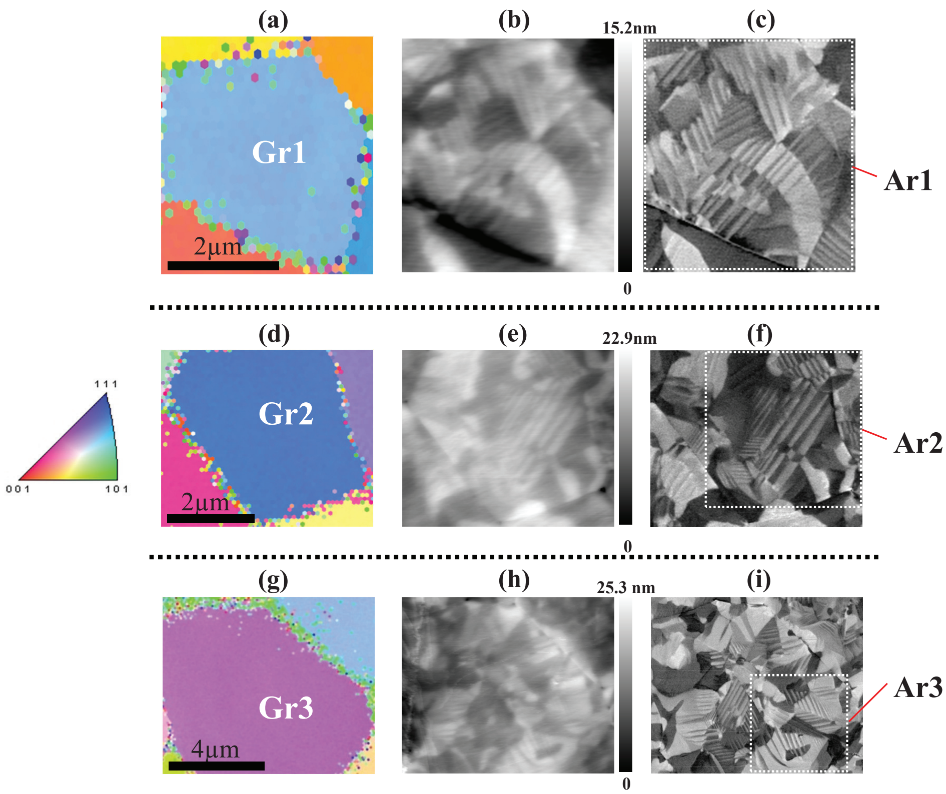

Figure 3.5: Characterization of the three distinct regions of interest through (a), (d), (g) EBSD inverse pole figures, (b), (e), (h) AFM topography images, and (c), (f), (i) PFM images.

and (i) VPFM images, for three distinct areas of interest. Note that the surfaces were normally flat, so the AFM topography is not expected to show significant features. The topography data confirm flatness to within about 25 nm and also show some surface indentations that roughly match the underlying domain structure, probably due to a slight effect of domain orientation on the polishing process. Domain evolution was studied in area Ar1 in grain Gr1, area Ar2 marked in grain Gr2, and area Ar3 in grain Gr3 as shown in figure 3.5.

3.3 Theoretical background

The "primary principle" of ferroelectric domain switching and Hwang's switching criterion (equation 1.5) [6] were introduced in chapter 1. When only mechanical stress is considered, the criterion becomes

$$\sigma_{jk} \Delta \varepsilon_{jk} \geq G_c \, . \tag{3.1}$$

Suppose a steadily increasing stress of the form $\lambda\sigma_{jk}$ is applied, where λ is a scalar multiplier, Hwang's criterion suggests that the most favourable switching event (that with the greatest value of $\sigma_{jk}\Delta\varepsilon_{jk}$) to happen at the lowest stresses (least value of λ). Less favourable switching should occur at higher stresses, and unfavourable switching ($\sigma_{jk}\Delta\varepsilon_{jk} < 0$) should not happen. Using this criterion, similar macroscopic behaviour to actual measurements such as the stress-strain curve can be reproduced [6]. In this chapter, the validity of the energetic criteria is tested at the microscopic scale.

The applied stress σ_{jk} in our experiment was a uniaxial compression along the x_2 axis in the instrument coordinate system. The resulting $\Delta\varepsilon_{jk}$ was first found in local crystallographic coordinates ($\Delta\varepsilon'_{jk}$) by interpreting the PFM measurements and EBSD data. The EBSD data also provided the three Euler angles ($\varphi_1, \Phi, \varphi_2$) where φ_1 is the angle of anticlockwise rotation about the x_3 axis in instrument co-ordinates, Φ is a subsequent clockwise rotation about the new x_1 axis and φ_2 is an anticlockwise rotation about the resulting x_3 axis. See the instrument coordinate system in figure 3.3(b), and coordinate transformations in figure 2.10 in chapter 2. Hence a rotation matrix $\boldsymbol{R}$ is defined, such that the strain in the instrument coordinate system $\boldsymbol{\varepsilon}$ can be obtained by $\boldsymbol{\varepsilon} = \boldsymbol{R}\boldsymbol{\varepsilon}'\boldsymbol{R}^{\mathrm{T}}$, where $\boldsymbol{\varepsilon}'$ is in the crystal coordinate system. The applied stress is assumed to be pure σ_{22} with a negative sign since only compressive stresses are applied. Then the most favourable switching system was simply that with the most negative value of $\Delta\varepsilon_{22}$ and so forth.

Since changes in spontaneous strain state are concerned, the strain states can be defined relative to an equal volume cubic reference state. In the tetragonal phase, the three spontaneous strain states $\boldsymbol{\varepsilon}'_{\mathbf{a}}, \boldsymbol{\varepsilon}'_{\mathbf{b}}, \boldsymbol{\varepsilon}'_{\mathbf{c}}$ corresponding to polarization vectors $\mathbf{P}'$ can then be written as:

$$\boldsymbol{\varepsilon}'_{\mathbf{a}} = \alpha \begin{bmatrix} 1 & 0 & 0 \\ 0 & -1/2 & 0 \\ 0 & 0 & -1/2 \end{bmatrix}, \text{ for } \mathbf{P}'_{\mathbf{a}} = \pm P_{\mathrm{t}} \begin{bmatrix} 1 \\ 0 \\ 0 \end{bmatrix},$$

$$\boldsymbol{\varepsilon}'_{\mathbf{b}} = \alpha \begin{bmatrix} -1/2 & 0 & 0 \\ 0 & 1 & 0 \\ 0 & 0 & -1/2 \end{bmatrix}, \text{ for } \mathbf{P}'_{\mathbf{b}} = \pm P_{\mathrm{t}} \begin{bmatrix} 0 \\ 1 \\ 0 \end{bmatrix}, \quad (3.2)$$

$$\boldsymbol{\varepsilon}'_{\mathbf{c}} = \alpha \begin{bmatrix} -1/2 & 0 & 0 \\ 0 & -1/2 & 0 \\ 0 & 0 & 1 \end{bmatrix}, \text{ for } \mathbf{P}'_{\mathbf{c}} = \pm P_{\mathrm{t}} \begin{bmatrix} 0 \\ 0 \\ 1 \end{bmatrix},$$

where α and P_{t} are material properties. Meanwhile, in the rhombohedral phase, there are four distinct spontaneous strain states. Let us label them $\boldsymbol{\varepsilon}'_{\mathbf{d}} \ldots \boldsymbol{\varepsilon}'_{\mathbf{g}}$ as follows:

$$\boldsymbol{\varepsilon}'_{\mathbf{d}} = \beta \begin{bmatrix} 0 & 1 & 1 \\ 1 & 0 & 1 \\ 1 & 1 & 0 \end{bmatrix}, \text{ for } \mathbf{P}'_{\mathbf{d}} = \pm P_{\mathrm{r}} \begin{bmatrix} 1 \\ 1 \\ 1 \end{bmatrix},$$

$$\boldsymbol{\varepsilon}'_{\mathbf{e}} = \beta \begin{bmatrix} 0 & -1 & -1 \\ -1 & 0 & 1 \\ -1 & 1 & 0 \end{bmatrix}, \text{ for } \mathbf{P}'_{\mathbf{e}} = \pm P_{\mathrm{r}} \begin{bmatrix} -1 \\ 1 \\ 1 \end{bmatrix},$$

$$(3.3)$$

$$\boldsymbol{\varepsilon}'_{\mathbf{f}} = \beta \begin{bmatrix} 0 & 1 & -1 \\ 1 & 0 & -1 \\ -1 & -1 & 0 \end{bmatrix}, \text{ for } \mathbf{P}'_{\mathbf{f}} = \pm P_{\mathrm{r}} \begin{bmatrix} -1 \\ -1 \\ 1 \end{bmatrix},$$

$$\boldsymbol{\varepsilon}'_{\mathbf{g}} = \beta \begin{bmatrix} 0 & -1 & 1 \\ -1 & 0 & -1 \\ 1 & -1 & 0 \end{bmatrix}, \text{ for } \mathbf{P}'_{\mathbf{g}} = \pm P_{\mathrm{r}} \begin{bmatrix} 1 \\ -1 \\ 1 \end{bmatrix},$$

where β and P_r are material properties. Equations (3.2) and (3.3) will be used subsequently for computing $\Delta\varepsilon_{22}$.

3.4 Results

The main difference of domain evolution by mechanical stress, compared with the electrical switching studied in chapter 2, is that 180° domain switching is not induced by mechanical stress. This difference is illustrated in figure 3.6. Figures 3.6(a)–(d) show four PFM images taken from AR1 in figure 3.5 before mechanical loading, after compressive strains of 0.118%, 0.134%, and after unloading. Since the domain structures and their evolution processes in figures 3.6(a)–(d) are complex, some interesting parts are depicted in the schematics, see figures 3.6(e)–(f). Before applying compressive stress, the six needle-like non-180° domain structures can be seen from figures 3.6(a) and (e). These needle-like structures were broadened during mechanical loading, and some needles were merged together as figures 3.6(b)–(c) show. Compared to the broadening process, a lengthening process was not clearly observed. This may be because the tips of the needle-like domains were adjacent to a differently oriented domain or GB as is confirmed by the EBSD inverse pole figure in figure 3.5(a). By contrast with the active domain wall motion in non-180° domains, the curvy 180° domain walls marked in figure 3.6(e) were almost motionless during mechanical loading and unloading. Therefore, from figure 3.6 it can be confirmed that externally applied stress induces domain wall motion in non-180° domain structures. The domains in non-180° domain structures have different strain states, and hence one can be more favourable to grow than the other with respect to the applied stress. However, a 180° domain wall is normally not affected by mechanical stress since the domains have the identical strain states. Some subtle 180° domain switching driven by externally applied stress can be observed by PFM. Note the assumption that curvy

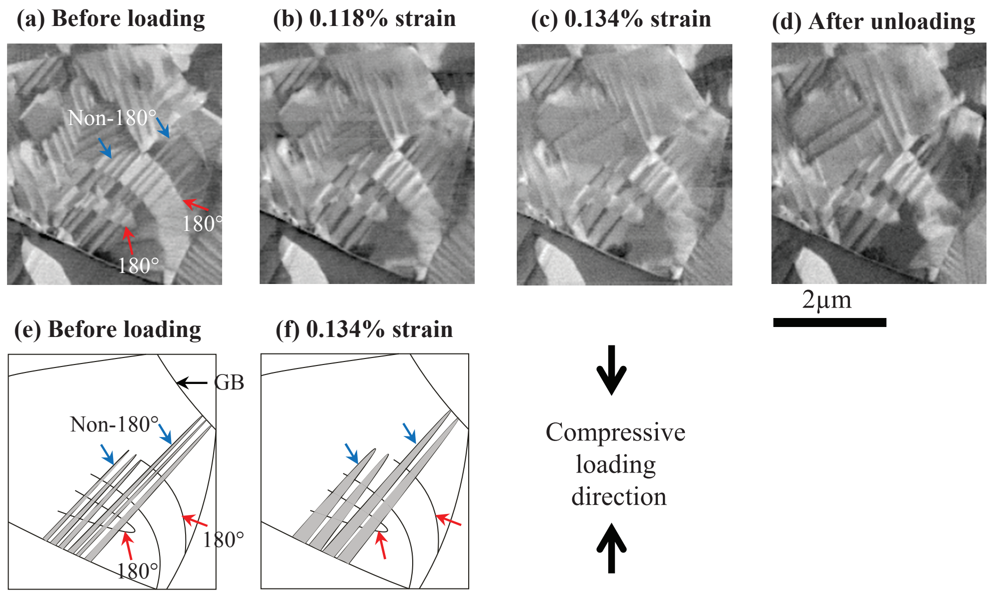

Figure 3.6: (a)–(d) PFM images showing domain evolution processes of non-180° under compressive loading. (e)–(f) Two schematics depict the broadening process of needle-like domain structures. See figures 3.5(a)–(b) for the clear grain boundaries. The images were taken from AR1 in figure 3.5.

lines are 180° domain wall and straight lines are non-180° domain wall in this PZT material will be confirmed by using AR-PFM in chapter 4.

Figures 3.7(a)–(d) show four PFM images corresponding to the area of sample surface marked Ar2 in figure 3.5. The images were taken before mechanical loading, after compressive strains of 0.118%, 0.134%, and after unloading, respectively. Two schematics in figures 3.7(e)–(f) represent the domain structures before loading and at a compressive strain level of 0.134%, clarifying domain evolution processes. The intersections of the $(01\bar{1})$, (101) and (110) planes with the viewing plane are shown for later use.

Several domain evolution processes were observed in this area, summarized as follows: Firstly, and perhaps the simplest of the domain evolution processes, can be seen in the centre of figure 3.7(a) where a coarse lamellar pattern is aligned with the (110) orientation; the width of a domain in dark contrast is indicated by label A1. This width gradually decreased during compression as figures 3.7(b) and (c) show. During unloading,

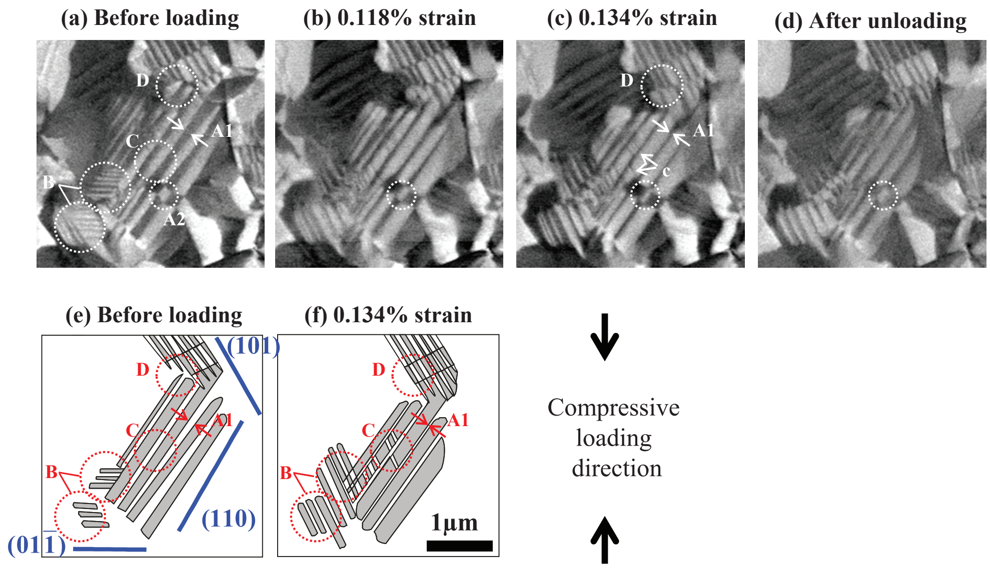

Figure 3.7: (a)–(d) PFM images showing domain evolution processes under compressive loading. (e)–(f) Two schematics depict key evolution processes such as the broadening of lamellae and overwriting of one lamellation by a differently oriented lamellation. The images were taken from AR2 in figure 3.5.

the width A1 increased towards the original value. This evolution process can be also observed in the region marked A2, see figures 3.7(a)–(d).

Secondly, the lamellae in region B aligned with $(01\bar{1})$ were overwritten by new lamellae in the (101) orientation. Overwriting took place when the compressive strain was less than 0.118%, but remained unchanged during loading to the 0.134% strain level and after unloading. The new domain structure can be clearly observed in figures 3.7(c) and (d).

Thirdly, fine needle-like structures aligned with the (101) plane emerged in region C when strain ≤ 0.118%. More needle-like structures, marked c in figure 3.7(c), can be seen after increasing the strain level to 0.134%. The PFM image taken after unloading is not clear enough to identify these fine needle-like structures. In both the second and third processes there is similar evolution of domain patterns: existing lamellae aligned with the $(01\bar{1})$ and (110) planes were overwritten by new lamellae aligned with the (101) orientation. However, in the third process, the domains did not erase the existing

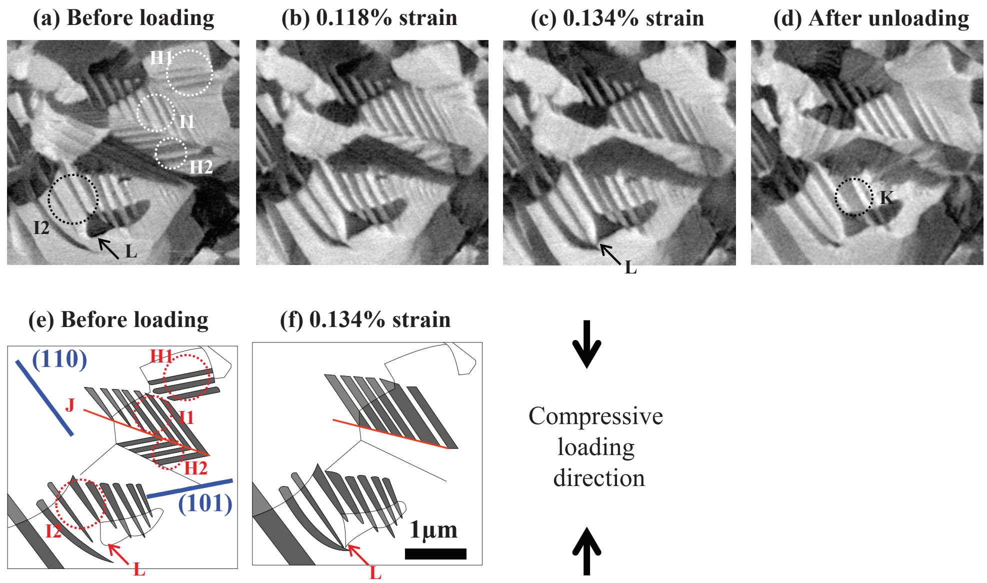

Figure 3.8: (a)–(d) PFM images showing the evolution process of the herringbone-like domain pattern under compressive loading. (e)–(f) Two schematics depict key evolution processes such as the broadening of needle-like domains and domain wall motion in the herringbone-like domain structure. The images were taken from AR3 in figure 3.5.

lamellation in (110) orientation, but instead appeared as fine needles within larger lamellae.

Fourthly, in the region marked D, two adjacent lamellations aligned with the (101) and (110) planes are seen. The lamellation aligned with (101) grows along its length while the (110) lamellation retreats. This is somewhat similar to the second process introduced earlier, except that here a gradual motion of the boundary between two distinct regions is seen. The process did not reverse upon unloading.

The domain evolution processes for the area Ar3 of figure 3.5 are shown in figures 3.8(a)–(d); simplified diagrams are again shown in figures 3.8(e)–(f). Here, the lamellations in H1, I1 and H2 compose a herringbone pattern before loading. This herringbone-like domain structure is a rank-2 pattern; the interface between the rank-1 lamellations is labelled J.

In figure 3.8, the evolution process can be summarized as follows. The domains in dark contrast in H1 and H2 disappeared while the domains in dark contrast in I1 and I2 broadened. When the strain level reached 0.134%, the lamellar patterns aligned with the (101) plane are no longer visible in H1 and H2. Meanwhile, the boundary J between the two lamellations I1 and H2 in figure 3.8(e) has moved downward; this did not return after unloading. Hence, the lamellation aligned with (110) in the area I1 has grown, overwriting the lamellation in (101) orientation in the area H2. It is interesting to note that after unloading, the needle-like structures marked K became merged together during unloading, see figure 3.8(d). Finally, the curvy 180° domain wall marked L, seen in figures 3.8(a)–(d), was almost motionless during mechanical loading, though a small region near the tip of the arrow marking L changed shape during loading and returned to its initial state upon unloading.

3.5 Discussion

From figure 3.7, four distinct domain evolution processes were identified, the first involving only the broadening of domains in a rank-1 lamellation. The other three processes concerned competition between two differently oriented lamellations. In particular, lamellations aligned with (101) grew over the other lamellations aligned with either $(01\bar{1})$ or (110). Let us consider whether these evolution mechanisms appear consistent with the primary principle of switching, and to what extent they follow Hwang's switching criterion. To do this, first note that the near-morphotropic PZT may exhibit either tetragonal or rhombohedral phases. The axes of polarization in the tetragonal and rhombohedral systems are given in table 3.1, labelling the spontaneous strain variants **a**…**g** as in equations (3.2) and (3.3). From the point of view of ferroelastic switching, the polarization states of the individual crystal variants do not enter into the energetic balance of equation (3.1); only the spontaneous strain states are relevant. Each pairing of spontaneous strain variants specifies compatible domain wall orientations (solutions of equation (1.1)) as shown in table 3.2.

Table 3.1: Notation for 7 pairs of polarization direction.

Tetragonal	Rhombohedral
$\mathbf{a} = \pm[100]$	$\mathbf{d} = \pm[111]$
$\mathbf{b} = \pm[010]$	$\mathbf{e} = \pm[1\bar{1}\bar{1}]$
$\mathbf{c} = \pm[001]$	$\mathbf{f} = \pm[11\bar{1}]$
	$\mathbf{g} = \pm[1\bar{1}1]$

Table 3.2: Compatible domain wall orientations for domain pairs in the tetragonal and rhombohedral systems.

Tetragonal		Rhombohedral	
Pairing	Domain wall	Pairing	Domain wall
$\mathbf{a}\vert\mathbf{b}$	$(110)/(1\bar{1}0)$	$\mathbf{d}\vert\mathbf{e}$	$(011)/(100)$
$\mathbf{a}\vert\mathbf{c}$	$(101)/(10\bar{1})$	$\mathbf{d}\vert\mathbf{f}$	$(110)/(001)$
$\mathbf{b}\vert\mathbf{c}$	$(011)/(01\bar{1})$	$\mathbf{d}\vert\mathbf{g}$	$(101)/(010)$
		$\mathbf{e}\vert\mathbf{f}$	$(10\bar{1})/(010)$
		$\mathbf{e}\vert\mathbf{g}$	$(1\bar{1}0)/(001)$
		$\mathbf{f}\vert\mathbf{g}$	$(01\bar{1})/(100)$

Considering the first process of domain evolution, the broadening of domains labelled A1 in figure 3.7 involves the motion of (110) domain walls. Table 3.2 indicates that the process involves the domain pair $\mathbf{a}\,|\,\mathbf{b}$ in the tetragonal phase, or $\mathbf{d}\,|\,\mathbf{f}$ in the rhombohedral phase. This illustrates the difficulty of interpretation of domain patterns in near-morphotropic PZT as domain patterns from either phase can appear identical in a PFM scan. Next, consider the $\Delta\varepsilon_{22}$ values associated with the motion of the domain wall. Table 3.3 shows the ε_{22} for each domain type, and table 3.4 represents the $\Delta\varepsilon_{22}$ values for each switching process, which were computed by making use of the three Euler angles (53.7°, 131.2°, 35.3°) for this grain, from EBSD data. The switching processes are ordered from most favourable (most negative $\Delta\varepsilon_{22}$) to least favourable. Unfortunately, the PFM contrast in our system is not able to differentiate whether the broadening process was $\mathbf{a} \to \mathbf{b}$ or $\mathbf{b} \to \mathbf{a}$ in the tetragonal system ($\mathbf{d} \to \mathbf{f}$ or $\mathbf{f} \to \mathbf{d}$ in rhombohedral), but note that $\mathbf{b} \to \mathbf{a}$ and $\mathbf{f} \to \mathbf{d}$ are among the most favourable switching processes according to Hwang's criterion. Thus, although the first domain evolution process was the simplest observed, the evidence does not enable us to verify the primary principle of switching.

Table 3.3: The list of ε_{22} for each polarization in tetragonal and rhombohedral in the area Ar2 in figure 3.5.

Phase	Polarization	ε_{22}
Tetragonal	$\pm[100]/\mathbf{a}$	-0.4875α
	$\pm[010]/\mathbf{b}$	0.4360α
	$\pm[001]/\mathbf{c}$	0.0516α
Rhombohedral	$\pm[111]/\mathbf{d}$	-0.9915β
	$\pm[1\bar{1}\bar{1}]/\mathbf{e}$	-0.9245β
	$\pm[11\bar{1}]/\mathbf{f}$	0.7035β
	$\pm[1\bar{1}1]/\mathbf{g}$	1.2126β

Table 3.4: The $\Delta\varepsilon_{22}$ values for each switching process in area Ar2 in figure 3.5, ordered from most energetically favourable to least energetically favourable.

Tetragonal		Rhombohedral	
$\mathbf{b} \to \mathbf{a}$	-0.9235α	$\mathbf{g} \to \mathbf{d}$	-2.2041β
$\mathbf{c} \to \mathbf{a}$	-0.5391α	$\mathbf{g} \to \mathbf{e}$	-2.1371β
$\mathbf{b} \to \mathbf{c}$	-0.3844α	$\mathbf{f} \to \mathbf{d}$	-1.6950β
$\mathbf{c} \to \mathbf{b}$	0.3844α	$\mathbf{f} \to \mathbf{e}$	-1.6280β
$\mathbf{a} \to \mathbf{c}$	0.5391α	$\mathbf{g} \to \mathbf{f}$	-0.5091β
$\mathbf{a} \to \mathbf{b}$	0.9235α	$\mathbf{e} \to \mathbf{d}$	-0.0670β
		$\mathbf{d} \to \mathbf{e}$	0.0670β
		$\mathbf{f} \to \mathbf{g}$	0.5091β
		$\mathbf{e} \to \mathbf{f}$	1.6280β
		$\mathbf{d} \to \mathbf{f}$	1.6950β
		$\mathbf{e} \to \mathbf{g}$	2.1371β
		$\mathbf{d} \to \mathbf{g}$	2.2041β

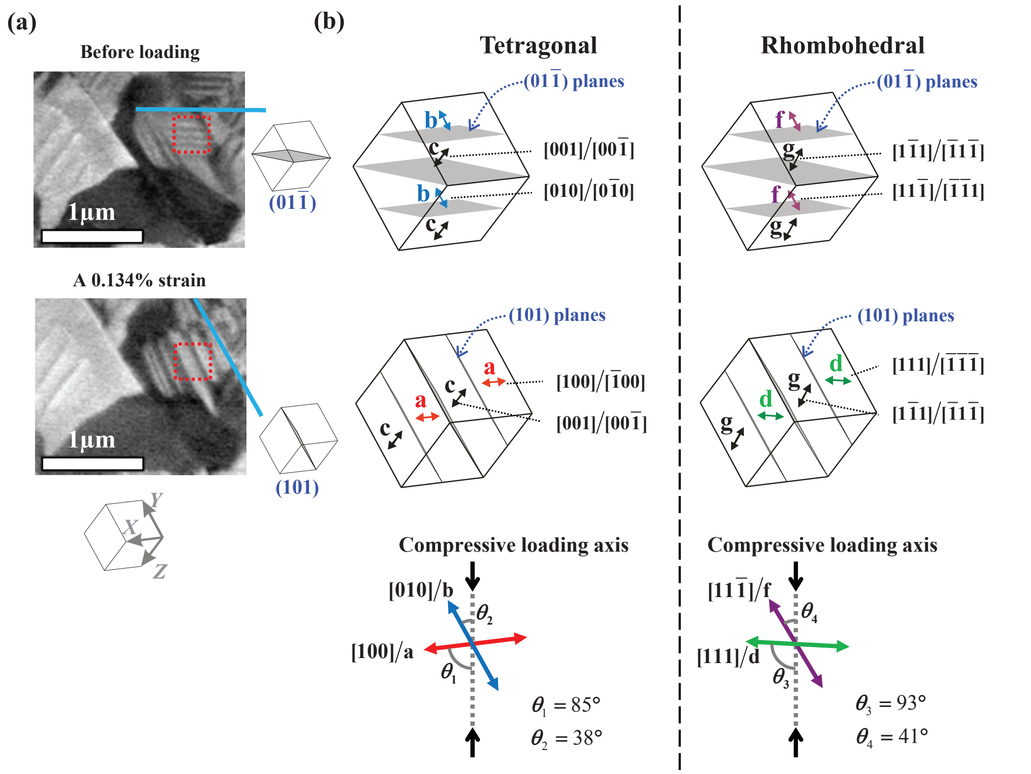

Figure 3.9: (a) Identifying the crystallographic planes of lamellar patterns in figure 3.7 using PFM and EBSD data. (b) Comparison of the angle between the compressive loading axis and polarization axis in the ferroelastic domain structures.

Moving on to the second domain evolution process, the overwriting of one lamellation by a differently oriented lamellation has the advantage for the analysis that it involves more than two spontaneous strain states: this provides greater certainty over which switching processes are happening and hence a clearer test of the primary principle.

Figure 3.9(a) shows enlarged views of the lower part of region B from figures 3.7(a) and (c), along with a three-dimensional view of the (01$\bar{1}$) and (101) planes. The regions marked by a red dotted line highlight the lamellation aligned with (01$\bar{1}$) which is overwritten by a lamellation aligned with (101). Since we do not have measurements to confirm whether this grain is in the tetragonal or rhombohedral phase, the analysis was carried out for both cases. In the tetragonal phase there are only three distinct spontaneous strain states, hence the two differently oriented lamellations must have one spontaneous strain state in common. The evolution process illustrated in figure 3.9 may be written $\mathbf{b}\,|\,\mathbf{c} \rightarrow \mathbf{a}\,|\,\mathbf{c}$ with state **c** in common to both lamellations. Hence the net effect is the conversion $\mathbf{b} \rightarrow \mathbf{a}$, and referring to table 3.4 shows that this is the most favourable switching process according to Hwang's criterion. Note that this statement about the net effect of overwriting assumes that the proportions of the domains in each lamellation are approximately 1:1. It is not possible to be certain of these proportions from the observed cross-section, although the regions of light and dark contrast in the lamellations appear approximately equal.

Considering the case of rhombohedral crystal structure, the corresponding process is $\mathbf{f}\,|\,\mathbf{g} \rightarrow \mathbf{d}\,|\,\mathbf{g}$ with spontaneous strain state **g** in common to both lamellations, see figure 3.9(b). The net effect is then to convert $\mathbf{f} \rightarrow \mathbf{d}$, again among the most favourable switching processes by Hwang's criterion. In either case, the primary principle of energy release by the external loads is followed. Since the longest axis of the unit cell in tetragonal and rhombohedral ferroelectrics is often aligned with the spontaneous polarization, the primary principle is often expressed as the statement that uniaxial compressive stress tends to align the polarization vectors in a plane orthogonal to the mechanical loading axis [6,8,18,28,29]. This is consistent with the observations here, see figure 3.9(b).

It is interesting to note that the $(01\bar{1})$ plane is very close to orthogonal to the compressive loading axis. This plane contains both the [100] and $[\bar{1}00]$ polarization vectors in the tetragonal phase, and the [111], $[\bar{1}\bar{1}\bar{1}]$, $[\bar{1}11]$, and $[1\bar{1}\bar{1}]$ polarization vectors in the rhombohedral phase. Thus, these vectors are also very close to orthogonal to the loading axis, noting that there are small differences depending on specific vectors. Ferroelastic domain walls cannot be generated along the plane parallel to their polarization vectors under compatibility conditions, in either the tetragonal and rhombohedral phases. Thus, none of these polarization vectors can compose the ferroelastic domain walls in the $(01\bar{1})$ plane, and hence the lamellation aligned with this plane would not be favoured to grow by the compressive loading, compared to the other differently oriented lamellations having one of these polarization vectors. As a result, the lamellation in the $(01\bar{1})$ plane was overwritten by another lamellation in (101) plane.

In general, a ferroelastic domain wall aligned very close to orthogonal with respect to the compressive loading axis is likely to disappear or be overwritten by a differently oriented lamellation. However, this should not be judged only from two-dimensional orientation observed in the viewing plane because the three-dimensional orientation of a domain wall cannot be inferred from the two-dimensional view.

Having established that the overwriting process follows the primary principle of switching in an overall sense, it is of interest to examine more closely the processes that occur as one lamellation grows over another. Overwriting a lamellar pattern by a differently oriented lamellar pattern involves multiple types of non-180° switching. A schematic of the overwriting process is shown in figure 3.10. In the tetragonal crystal system, overwriting $\mathbf{b}\,|\,\mathbf{c} \rightarrow \mathbf{a}\,|\,\mathbf{c}$ involves four distinct events $\mathbf{b} \rightarrow \mathbf{a}$, $\mathbf{c} \rightarrow \mathbf{a}$, $\mathbf{b} \rightarrow \mathbf{c}$ and $\mathbf{c} \rightarrow \mathbf{c}$, the last of which involves no change in spontaneous strain, and hence no ferroelastic switching, although it could involve 180° switching. From table 3.4 it can be seen that all three ferroelastic switching events are energetically favourable. But it is of interest to note that equation (3.1) suggests that the most favourable event ($\mathbf{b} \rightarrow \mathbf{a}$) would occur at a lower stress value, and hence at an earlier stage of loading, than the other events. In practice the switching events occur together, co-operatively, enabling the material to maintain a low energy lamellar configuration. If the same overwriting process is analysed in terms of rhombohedral crystal variants, it is found that switching event $\mathbf{f} \rightarrow \mathbf{g}$ is required, which is energetically unfavourable, according to Hwang's criterion.

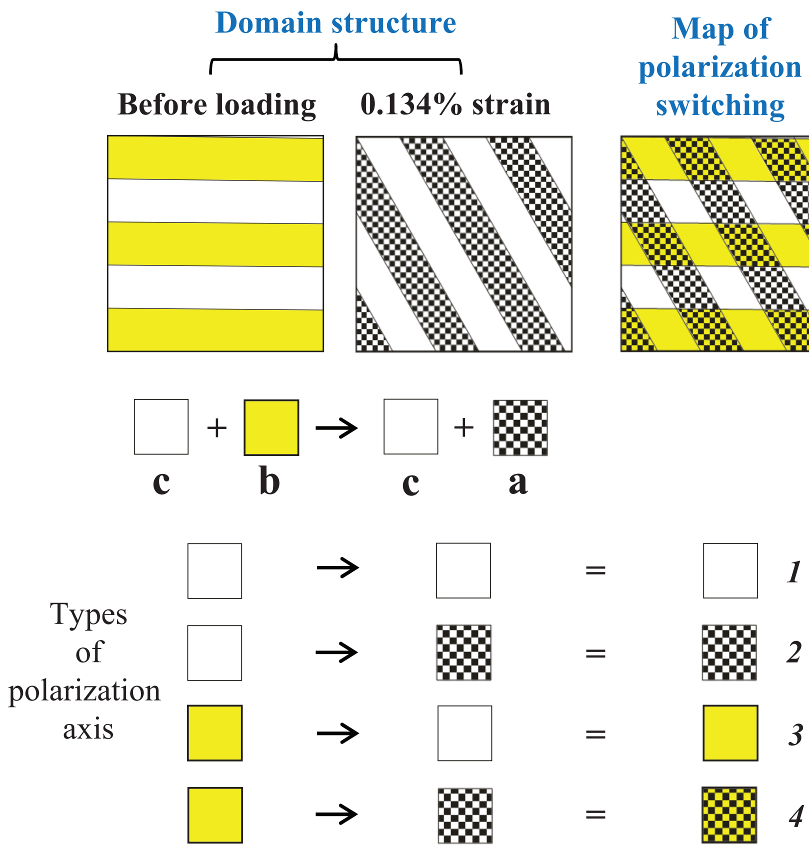

Figure 3.10: Overwriting a lamellation by differently oriented lamellation. This overwriting process involves three types of non-180° polarization switching, labeled as *2*, *3*, and *4*.

In terms of the lamellations involved, the third and fourth domain evolution processes are similar, both introducing (101) oriented domain walls into an existing (110) oriented lamellation. The fourth domain evolution process is analysed in more detail as this reveals the requirement for co-operative switching events. This is again an overwriting process, which can be expressed as $\mathbf{b}\,|\,\mathbf{a} \to \mathbf{c}\,|\,\mathbf{a}$ if in the tetragonal system, $\mathbf{f}\,|\,\mathbf{d} \to \mathbf{g}\,|\,\mathbf{d}$ if rhombohedral, see figure 3.11. From table 3.4 it can be seen that regardless of whether the grain is tetragonal or rhombohedral, an energetically unfavourable switching event occurs. Specifically, if in the tetragonal phase, event $\mathbf{a} \to \mathbf{c}$ occurs, but if in the rhombohedral phase $\mathbf{d} \to \mathbf{g}$ occurs. These events do not follow Hwang's criterion, and individually contrary to the primary principle. However, if the phase is tetragonal, the net effect of overwriting is the conversion $\mathbf{b} \to \mathbf{c}$ which is

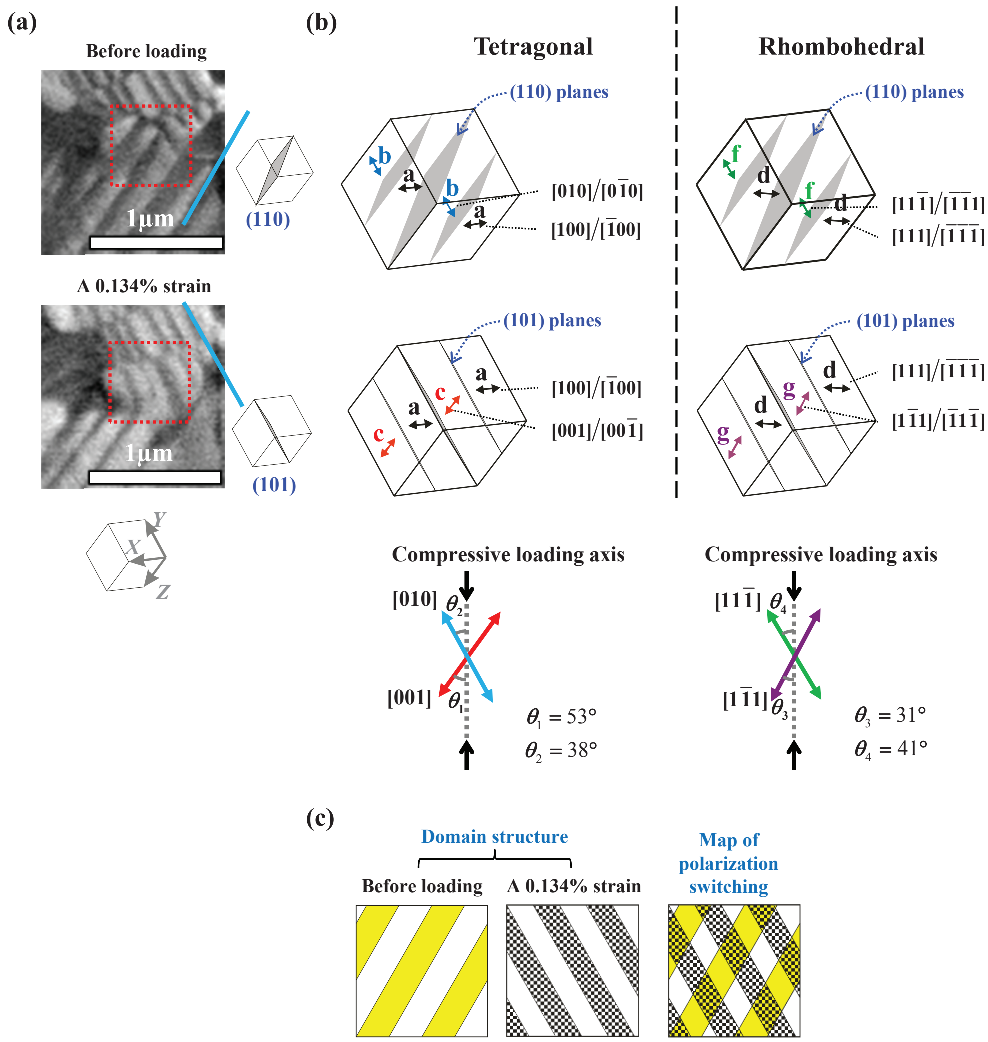

Figure 3.11: (a) Identifying the crystallographic planes of lamellar patterns in figure 3.7 using PFM and EBSD data. (b) Identifying polarization directions in each plane. (c) The overwriting process involves three types of ferroelastic switching.

energetically favourable. This observation can be summarized by the statement that the primary principle of energetically favourable switching processes appears to hold in an overall sense, while local switching events may not follow the principle as expressed in Hwang's criterion.

Figure 3.12 shows a further illustration of the same points, this time in grain Gr3 of figure 3.5. The Euler angles, and $\Delta\varepsilon_{22}$ values for this grain are given in table 3.6. An overwriting process in which (110) lamellations grow while (101) lamellations disappear was observed. The individual switching events are illustrated in figure 3.12(b). If the

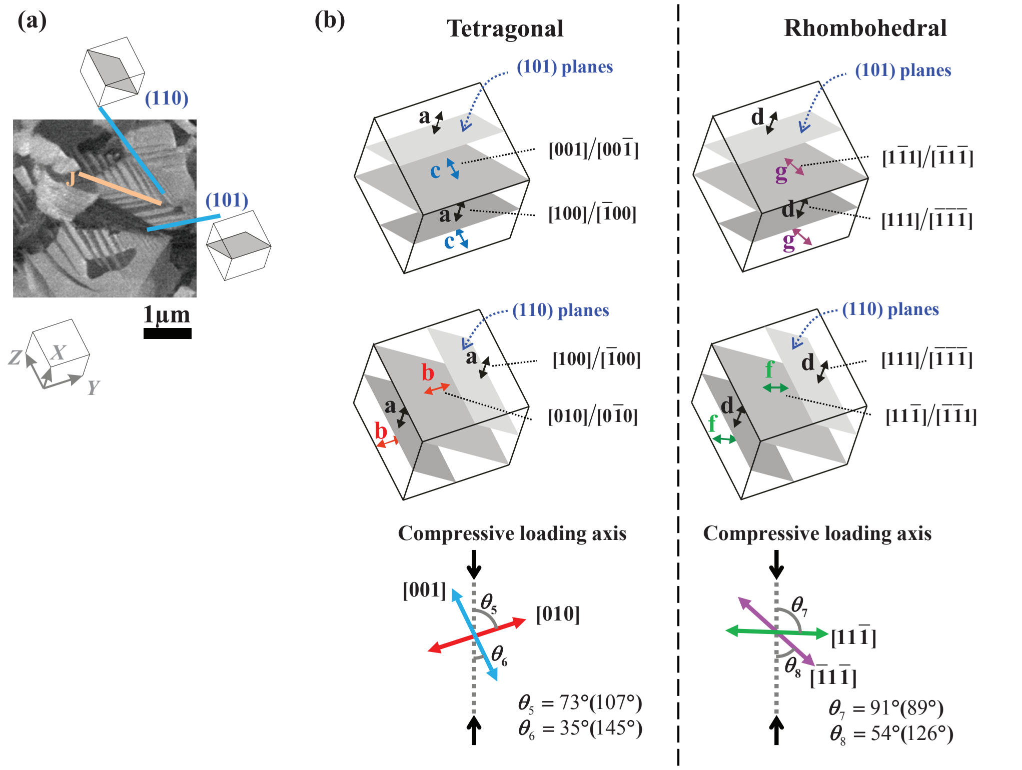

Figure 3.12: (a) Identifying the crystallographic planes of lamellar patterns in figure 3.8 using PFM and EBSD data. (b) Comparison of the angle between the compressive loading axis and polarization axis in the ferroelastic domain structures.

grain is tetragonal, the lamellar patterns evolved by the domain switching process $\mathbf{a}\,|\,\mathbf{c} \rightarrow \mathbf{a}\,|\,\mathbf{b}$, where **a** is in common in both lamellations. Thus, the net effect of domain evolution was determined by the strain states of **c** and **b**. Meanwhile, in a rhombohedral the domains evolved by $\mathbf{d}\,|\,\mathbf{g} \rightarrow \mathbf{d}\,|\,\mathbf{f}$, where **d** exists in both lamellations (110) and (101). Accordingly, the net movement of domain patterns is determined by the competition between the strain states **g** and **f**. Then, using table 3.5 and 3.6, it becomes clear that the net effect of the domain evolution process is consistent with the primary principle and with Hwang's criterion. If the grain is tetragonal, each individual switching event is energetically favourable. But if the grain is rhombohedral, then at least some of the individual switching events are energetically unfavourable.

Table 3.5: The list of ε_{22} for each polarization in tetragonal and rhombohedral in the area Ar3 in figure 3.5.

Phase	Polarization	ε_{22}
Tetragonal	$\pm[100]/\mathbf{a}$	-0.1325α
	$\pm[010]/\mathbf{b}$	-0.3765α
	$\pm[001]/\mathbf{c}$	0.5090α
Rhombohedral	$\pm[111]/\mathbf{d}$	1.5666β
	$\pm[1\bar{1}\bar{1}]/\mathbf{e}$	-0.6253β
	$\pm[11\bar{1}]/\mathbf{f}$	-0.9985β
	$\pm[1\bar{1}1]/\mathbf{g}$	0.0572β

Table 3.6: The list of $\Delta\varepsilon_{22}$ for ferroelastic switching events in the area Ar3 in figure 3.5 with Euler angles (296.4°, 113.7°, 20.9°).

Tetragonal		Rhombohedral	
$\mathbf{c} \rightarrow \mathbf{b}$	-0.8855α	$\mathbf{d} \rightarrow \mathbf{f}$	-2.5651β
$\mathbf{c} \rightarrow \mathbf{a}$	-0.6415α	$\mathbf{d} \rightarrow \mathbf{e}$	-2.1919β
$\mathbf{a} \rightarrow \mathbf{b}$	-0.2440α	$\mathbf{d} \rightarrow \mathbf{g}$	-1.5094β
$\mathbf{b} \rightarrow \mathbf{a}$	0.2440α	$\mathbf{g} \rightarrow \mathbf{f}$	-1.0557β
$\mathbf{a} \rightarrow \mathbf{c}$	0.6415α	$\mathbf{g} \rightarrow \mathbf{e}$	-0.6825β
$\mathbf{b} \rightarrow \mathbf{c}$	0.8855α	$\mathbf{e} \rightarrow \mathbf{f}$	-0.3732β
		$\mathbf{f} \rightarrow \mathbf{e}$	0.3732β
		$\mathbf{e} \rightarrow \mathbf{g}$	0.6825β
		$\mathbf{f} \rightarrow \mathbf{g}$	1.0557β
		$\mathbf{g} \rightarrow \mathbf{d}$	1.5094β
		$\mathbf{e} \rightarrow \mathbf{d}$	2.1919β
		$\mathbf{f} \rightarrow \mathbf{d}$	2.5651β

The difference between Hwang's switching criterion and the actually observed evolution process of domain patterns is compared using a schematic stress versus strain curve in figure 3.13. First of all, in Hwang's switching criterion the most favourable switching $\mathbf{c} \rightarrow \mathbf{b}$ in tetragonal in table 3.6 occurs first during compressive loading process. And then the less favourable switching $\mathbf{c} \rightarrow \mathbf{a}$ and $\mathbf{a} \rightarrow \mathbf{b}$ follow as the stress is steadily increased. However, in the actual evolution process that includes broadening and lengthening of lamellation, and overwriting process between lamellar patterns, the stress

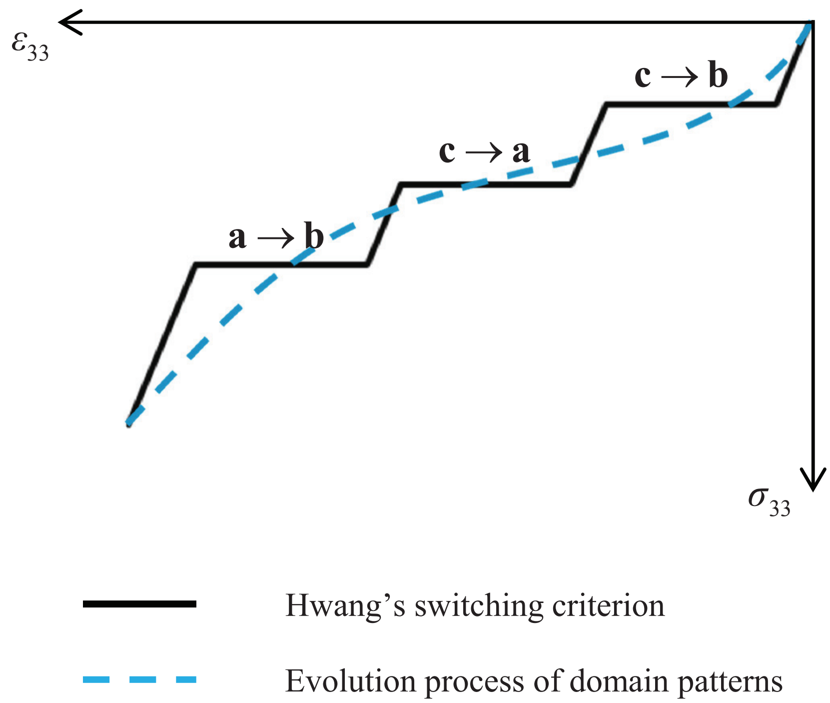

Figure 3.13: A schematic comparison of stress and strain curve for Hwang's switching criterion and for the actual evolution process of domain patterns.

vs. strain curve would not be stepwise since multiple ferroelastic domain switching processes take place concurrently.

One striking feature of all the results is that only a small fraction of the surface appears to change by domain evolution during loading. This can be explained by considering that there is a difference in the constraint of switching between the volume and the surface. The surface is mechanically unconstrained producing plane stress conditions. Thus, at first sight, more switching may be expected near the surface. However, surface switching is strongly inhibited by electrically insulating conditions, and hence non-180° domain switching is limited. Note also that a very small fraction of the surface was sampled including only those grains where switching was most evident. Hence the measured macroscopic average strain change is not expected to correlate with the local strain change in the sampled regions. Instead, a strain change greater than the macroscopic average could be expected in the localised regions where significant domain evolution occurs. For example, in figure 3.7(a) the strain induced by the broadening of domain bands in region C can be estimated as the product of volume fraction change and $\Delta\varepsilon_{22}$. Taking the transformation to be the most favourable switching system in the tetragonal phase, assuming volume fraction change of 11.9% and using $\alpha = 0.02$ gives a strain change of 0.22% for this region. Meanwhile the macroscopic strain change was 0.134% of which 0.047% elastic strain is estimated, leaving a strain due to switching events of 0.087%. Hence the local switching strain in this region was about 2.5 times the macroscopic average.

In summary, the evidence of the observations supports the statement that the net effect of domain evolution is consistent with the primary principle of switching. However, there is also clear evidence that local switching processes do not necessarily follow this principle. Instead, processes occur that allow the evolution of pre-existing patterns of domains, consistent with models of pattern evolution in ferroelectrics [85–87].

3.6 Conclusion

Ferroelastic domain evolution under compressive loading was studied with a near-morphotropic polycrystalline PZT bulk ceramic using VPFM. Diverse domain evolution processes were observed including broadening of lamellae within a rank-1 lamellation of alternating domains, and the motion of the boundary between lamellations in a rank-2 herringbone-like domain structure. In the latter process one lamellation was overwritten by a differently oriented lamellar pattern. Overwriting of one lamellation by another involved multiple switching processes. Analysis showed that the “primary principle”, requiring positive work from external loads during switching, is followed overall. However the overwriting process sometimes included a combination of energetically favourable and unfavourable transformations, contrary to the assumptions of macroscopic switching models that typically allow only energetically favourable events. The co-operative action of favourable and unfavourable switching events appears to happen because the process is significantly constrained by pre-existing domain structures. The resulting switching processes are thus better described as evolution of domain patterns. It was also observed that domain switching processes happened concurrently, rather than proceeding in order from most favourable to least favourable. The observations support and are consistent with modelling approaches that take account of the formation and evolution of patterns of domains.

In a later chapter, modelling methods will be explored that allows domain switching *via* a domain wall motion between the pre-existing domains by a compressive stress. However, it is also desirable to explore methods that could more reliably identify domain patterns. In the present chapter there was uncertainty between domains with similar VPFM contrast, and between tetragonal and rhombohedral phases. The next chapter explores AR-PFM that can be effectively used for identifying domain structures.